ChemElectroChem

Research Article
doi.org/10.1002/celc.202400318

Chemistry Europe
European Chemical Societies Publishing

www.chemelectrochem.org

Boosting the Oxygen Evolution Reaction Performance of Ni-Fe-Electrodes by Tailored Conditioning

Clara Gohlke,*[a] Julia Gallenberger,[b] Nico Niederprüm,[a] Hannah Ingendae,[a] Johann Kautz,[a] Jan P. Hofmann,[b] and Anna K. Mechler*[a]

To meet the rising demand for green hydrogen, efficient alkaline water electrolysis demands highly active and low-cost electrocatalysts for the oxygen evolution reaction (OER). We address this issue by focusing our work on optimizing the conditioning of promising Ni-(Fe)-based electrodes to improve their electrocatalytic performances. Systematic parameter variation for cyclic voltammetry conditioning revealed that a large potential window, low scan rate, and a high number of cycles result in improved activation. If the conditioning time is fixed, a high scan rate was found beneficial. A remarkable 47 ± 6 mV potential drop at 10 mA cm^{-2} was achieved for $Ni_{70}Fe_{30}$ when conditioning between −0.35–1.6 V at 100 mV s^{-1} for just 30 min. We could demonstrate that this activation persisted over 100 h at 100 mA cm^{-2}, underscoring its enduring efficacy. We suggest that this activation effect results from the growth of a hydrous hydroxide layer, which is supported by energy dispersive X-ray spectroscopy and X-ray photoelectron spectroscopy. Fe incorporation or dissolution played only a minor role in the differences in electrode activation, as demonstrated by variation of the Fe content in the electrolyte. Our work stresses the importance of conditioning in enhancing OER performance and explores how to improve the catalysts' effectiveness by tailoring oxides.

Introduction

To achieve the goal of green hydrogen as energy carrier, the oxygen evolution reaction (OER) in alkaline water electrolysis (AWE) requires a low-cost, highly efficient, and stable electrocatalyst. $NiFeO_xH_y$ is reported to be among the most active OER catalysts with an optimum Fe content of 15–60 wt%.[1–8] For synthesis, many different methods have been reported, such as electrodeposition,[9–11] Ni–Fe layered double hydroxides by hydrothermal treatment,[12] precipitation method,[13] alcohothermal method[14] and others, and Ni–Fe-based oxides by evaporation induced self-assembly, hard templating, and dip-coating.[15] Here, the critical factor affecting the catalytic activity is the surface structure. Li *et al.* for example suggested that the activity of their Ni_xFe_y hydroxide nanoclusters partly originated from their amorphous structure with oxygen vacancies.[16] This surface structure cannot only be tuned by the synthesis directly but also by pre-conditioning the catalyst, either chemically or electrochemically. Compared to the reported multi-step syntheses of metal oxide catalysts, *in-situ* conditioning of (pre)catalysts or bulk metals could save cost- and labor-intensive catalyst synthesis steps.

Conditioning of metals by potential cycling has already been outlined by Burke and O'Sullivan in 1981.[17] They introduced the duplex layer model to describe oxide films formed on metal surfaces during potential cycling, as illustrated in Figure 1. Here, the metal is covered by a thin (1–5 layers), compact, inner oxide layer, which is mainly anhydrous, and an outer oxide layer, which is extensively hydrated with both bound and trapped water. The outer oxide layer is reported to be catalytically active during OER.[17]

Son *et al.* compared the oxide structures resulting from conditioning by cyclic voltammetry (CV) and constant current operation and their activity in the OER. [18,19] CV conditioning resulted in a higher degree of oxidation to thicker NiO_xH_y layers for Ni-based substrates and, thus, showed a larger activity-

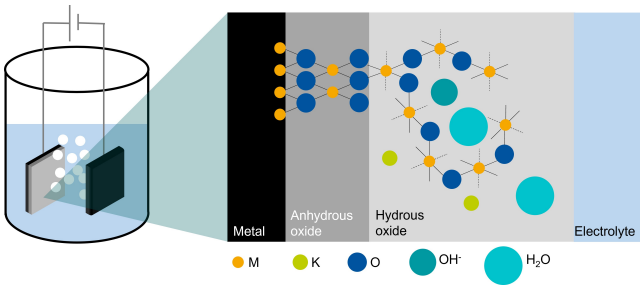

Figure 1. Schematic representation of the metal(oxide)/electrolyte interface on metals (M) according to the duplex layer model from Burke and O'Sullivan.[17]

[a] C. Gohlke, N. Niederprüm, H. Ingendae, J. Kautz, A. K. Mechler
Electrochemical Reaction Engineering (AVT.ERT)
RWTH Aachen University
Forckenbeckstraße 51, 52074 Aachen, Germany
E-mail: clara.gohlke@avt.rwth-aachen.de
anna.mechler@avt.rwth-aachen.de

[b] J. Gallenberger, J. P. Hofmann
Surface Science Laboratory
Department of Materials and Earth Sciences
Technical University of Darmstadt
Otto-Berndt-Straße 3, 64287 Darmstadt, Germany

Supporting information for this article is available on the WWW under https://doi.org/10.1002/celc.202400318

enhancing effect. This was attributed to the fact that at constant current conditions, further oxidation is limited by restricted ion movement through the anhydrous oxide layer. For CV, the cathodic sweep partially reduces the anhydrous layers and facilitates the rearrangement of the oxycation species to be more susceptible to oxidation and incorporation into the hydrous layer.[18,20–22] Lyons and coworkers built upon the duplex layer model and investigated the formation of hydrous oxide films on Fe and Ni under potential cycling by varying the number of cycles, scan rate, scan range, temperature, and KOH concentration.[20–24] Here, one key evaluation parameter was the oxide charge capacity, which was determined by the integration of the redox peaks of the M(II)/M(III) couple. The current response at a certain overpotential increased with the oxide charge capacity, saturating at approx. 0.01 C, independent of the applied potential.[20] With a larger number of cycles, the hydrous oxide film on Ni grew, saturating after approx. 250 cycles (−0.526–1.574 V *vs.* RHE, 40 mV s^{-1}) in 1 M NaOH. The reduced oxide growth rate with increasing film thickness was attributed to an increasing limitation of water and hydroxide ion transfer to the inner region of the oxide layer. Similar results were obtained for hydrous oxide films on Fe.[20,23] Regarding the influence of the scan rate, it was reported that for thin Ni-oxide films (< 60 cycles, −0.526-1.574 V *vs.* RHE, < 2 mC) the oxide charge capacity is independent of the scan rate between 2 V s^{-1} and 10 mV s^{-1}. Here, the redox reaction has sufficient time to extend throughout the entire dispersed hydrous oxide layer. For thicker Ni-oxide films (> 60 cycles, −0.526-1.574 V *vs.* RHE, > 2 mC), the oxide charge capacity increases linearly from 2 V s^{-1} to 50 mV s^{-1} and drastically below 50 mV s^{-1}. They suggest that for these thicker films, there is not enough time for the redox reaction to extend throughout the hydrous oxide layer.[20] The same relation was found for Fe-oxide films.[24] The works on hydrous oxide films on Fe further indicated that the oxide growth rate depends strongly on the upper and lower potential limit of the CV. The lower potential limit plays a crucial role in the extent of the partial reduction of the anhydrous oxide layer, which is supposedly maximized when the potential is reversed at the peak potential of the reduction of the compact anhydrous Fe-oxide layer (approx. −0.2 V *vs.* RHE).[21,23,24] Regarding the upper potential limit, different effects were reported. Increasing the upper potential of the CV could lead to a deeper oxygen penetration into the outer regions of the metal lattice, thickening the compact anhydrous layer.[21,22] It may also help to induce expansion and stress at the metal oxide interface, facilitating the uptake of excess oxygen. Plus, the reduction of the compact anhydrous oxide layer might become more challenging for more anodic upper potentials.[21,23] Consequently, Lyons and coworkers saw that the oxide charge capacity is increased with increasing the upper potential of the CV and that the optimal lower potential limit depends on the upper limit.[21,23]

Regarding oxide formation on Ni specifically, the Bode model describes its potential dependent phase transitions. In a simplified manner, hydrous α-Ni(OH)$_2$ oxidizes to γ-NiOOH and ages to anhydrous β-Ni(OH)$_2$, which can be oxidized to β-NiOOH.[2,25]

Besides the oxide formation, it is, nowadays, known that Fe is incorporated into Ni-based materials during aging with and without applied current or potential, but is significantly enhanced in electrochemical processes.[2,26] Klaus *et al.* reported the incorporation of about 15 at% Fe within 5 days of aging in unpurified 1 M KOH, resulting in a potential reduction of about 55 mV at 10 mA cm^{-2}.[2] It is important to point out that this Fe incorporation during the electrochemical operation was not considered in the earlier studies on the formation of hydrous oxide layers on Ni and Fe by Lyons *et al.*

More recently, studies on the electrochemical conditioning of steel electrodes as multi-element electrodes were published.[6,19,27–37] The goal was to find an efficient and cost-effective synthesis method for a highly active OER catalyst based on the abundant and low-cost raw material steel. Zhang *et al.* reported conditioning of 316 L steel by cathodization, which lowered the OER overpotential at 10 mA cm^{-2} by 70 mV. The activation was supposedly caused by an enrichment of Ni (oxy)hydroxide species on the surface.[33] Zhu *et al.* studied systematically the activation of 316 L stainless steel felt by CV conditioning. They focused on the variation of scan range, scan rate, and KOH concentration. Out of the three tested scan ranges 0.3–0.7 V, 0.7–1.7 V, and 0.3–1.7 V *vs.* RHE, the full scan range showed the largest activity enhancement. The investigation of different scan rates between 5 mV s^{-1} and 50 mV s^{-1} showed only a minor influence on the catalytic performance. Therefore, to save time, a scan rate of 50 mV s^{-1} was suggested. During activation, the composition of the surface layer changed, which was suggested to be the reason for the activity enhancement. The O-content increased due to oxide and hydroxide formation. Furthermore, Ni species were enriched, and the contents of Fe and Cr decreased.[34] Zuo *et al.* also identified that the CV conditioning with a larger potential window between −0.074–1.924 V compared to 0.924–1.924 V *vs.* RHE is more beneficial for the activation of SSM316 steel.[36] They attributed this to an increased Fe leaching at the lower potentials, which enlarges the surface area and results in an accumulation of OER-active Fe-incorporated NiOOH species. Additionally, they showed that re-activation by conditioning can result in stable OER performance over 300 h. Todoroki *et al.* had a closer look into the dissolution behavior of constituent elements of various stainless steel electrodes during CV cycling.[32] Regardless of the stainless-steel grade, constituents were dissolved in the order of Fe, Cr, Mn, and Ni in decreasing amounts. They suggested the Ni : Fe ratio as a key parameter to estimate the dissolution behavior of constituent elements. The higher the ratio, the more the dissolution is suppressed. Chatenet *et al.* reported that by aging or conditioning Ni–Fe-based alloys or oxides with initial Ni : Fe ratios between 0.14 to 250, the OER activity increases due to an optimized Ni : Fe ratio, which tends towards 2.5 to 5.[38] Based on the observed dissolution behavior, this *in-situ* conditioning of steel, however, needs to be reconsidered for industrial application since the industry is limited to a defined electrolyte quality and metal leaching might pose additional challenges.[39]

The presented studies investigated the conditioning of single- or multi-element electrodes regarding oxide growth on

Ni and Fe, and finding a highly active electrocatalyst from steel using *in-situ* conditioning. However, no study systematically correlated activation, surface changes, and electrochemical conditioning parameters for a model electrode with a Ni:Fe ratio in the optimum regime. Here, we present an ad hoc optimization of the electrochemical conditioning for such a Ni–Fe alloy electrode with 30 wt% Fe (31 at% Fe). The correlation between electrochemical protocol parameters and electrochemical activity is explored by varying the scan range, scan rate, hold times at the upper and lower potential limit, and the number of cycles. We present how these correlations are linked to the induced material changes, characterized by optical microscopy, scanning electron microscopy (SEM), energy dispersive X-ray spectroscopy (EDX), and X-ray photoelectron spectroscopy (XPS). To further understand the role of Fe in the activation, we show the influence of the Fe content in the electrode and electrolyte on the activation of the electrode. Lastly, we demonstrate the long-term effect of conditioning on the activity for $Ni_{70}Fe_{30}$ during 100 h of alkaline water electrolysis at 100 mA cm^{-2}.

Results and Discussion

Optimizing the Conditioning of $Ni_{70}Fe_{30}$

To study the influence of conditioning parameters on the OER performance of Ni–Fe-based electrodes, the conditioning of $Ni_{70}Fe_{30}$ ($Ni_{69at\%}Fe_{31at\%}$) as a model electrode was systematically optimized. As an evaluation parameter, the activation by conditioning was defined as the difference between the potentials at 10 mA cm^{-2} before and after conditioning, as defined in equation 1:

$$\Delta E_{10} = \bar{E}_{10,\,\text{after}} - \bar{E}_{10,\,\text{before}} \quad (1)$$

The potentials were averaged over the measurement of at least 100 s.An increase in activation will result in a negative ΔE_{10} ($E_{10,\text{after}} < E_{10,\text{before}}$). For better readability, $-\Delta E_{10}$ is plotted in the following.

First, the conditioning of the electrode under constant operation at open circuit potential (OCP) and 100 mA cm^{-2} was tested for reference. Figure 2a compares the activation from operation at OCP and 100 mA cm^{-2} to CV conditioning between different potential limits at 100 mV s^{-1}. All procedures were performed for 30 min. Conditioning the electrode at OCP or by CV cycling within the capacitive regime (0.5–1.0 V) did not show a significant activation (<10 mV). A slight activation of 10 ± 4 mV could be obtained when performing AWE at 100 mA cm^{-2}. This could be significantly improved to >14 mV by CV cycling in potential regions with relevant redox features of Ni or Fe. In alkaline electrolytes, the following redox potentials *vs.* RHE were reported: Ni(0) to Ni(II): 0.0–0.5 V,[20,40] Ni(II) to Ni(0): −0.2–0.1 V,[40] Ni(II) to Ni(III)/Ni(III) to Ni(II): 1.2–1.5 V,[20,41,42] Fe(0) to Fe(III) *via* Fe(I/II) and *vice versa* between −0.2–0.6 V.[24,43] These reported potentials correspond to the detected redox features when cycling $Ni_{99.99}$ and $Ni_{70}Fe_{30}$ in 1 M KOH at room temperature between −0.35–1.6 V at 100 mV s^{-1}, which can be seen in Figure S3. Based on previous reports,[18,20–22] we suggest the formation of a thin and compact anhydrous oxide layer with a hydrous oxide layer on top during AWE operation at 100 mA cm^{-2}. The diffusive oxidation process is, however, comparably slow at these conditions, and a stronger activation would only be visible after a longer conditioning time. At OCP and without the forced oxidative current, this surface oxidation process is much slower, resulting in no visible activation. During CV conditioning with relevant redox features of Ni or Fe, we assume that the activation is enhanced compared to the application of a constant oxidative current, because the respective hydrous oxides are formed more efficiently. The cathodic sweep reduces the anhydrous layer and facilitates the formation of a larger hydrous oxide layer during the anodic sweep.

When comparing the potential windows with the same size of 0.5 V, the largest activation of 25 ± 4 mV was achieved when cycling between −0.35-0.15 V, followed by 1.1–1.6 V, 1.0-1.5 V, and 0.5–1.0 V. This indicates that the application of low as well as high potentials seems to be beneficial for activation. At the low potentials between −0.35–0.15 V, the redox couples Ni(0)/Ni(II) and Fe(0) to Fe(III) *via* Fe(I/II) and *vice versa* are reported.[20,24,40,43] Thus, Fe dissolution might be favored in this regime, resulting in a higher surface area. This is supported by the qualitative comparison of the Ni^{2+}/Ni^{3+} redox peak area after conditioning between −0.35–1.6 V and 0.5–1.6 V at 100 mV s^{-1} for 30 min, as shown in Figure S4. The redox peak area increases during conditioning with either potential window, but more significantly when including the hydrogen evolution reaction (HER) (−0.35–1.6 V). This indicates more accessible Ni-oxide sites. Additionally to these oxidation processes, hydrolysis processes during HER are proposed to occur, contributing to the activation.[20,21,44,45] At the higher potentials, Ni(II) to Ni(III) oxidation and reduction take place between 1.2–1.5 V in 1 M KOH.[20,41,42] When including the OER in the CV conditioning, additional or different oxides might be formed or transformed, and a deeper oxygen penetration or uptake of excess oxygen might occur.[21–23] We can see that conditioning with a 0.5 V potential window within the M(0)/M(II)-regime results in a larger activation compared to cycling at higher potentials, where the oxidation of Ni(II)/Ni(III) and OER occurs. At higher potentials, the lower potential limit might be too high for sufficient reduction of the formed anhydrous oxides and the subsequent rearrangement of the oxide structure. This implies the importance of the lower potential limit over the upper potential limit.

As seen in Figure 2a, the activation was maximized to 47 ± 7 mV when enlarging the potential window and combining the HER and OER regime. This summarizes the above-stated observation and is in line with previous works on hydrous oxide films on Fe,[21] stating that a low lower and a high upper potential limit are beneficial for an efficient hydrous oxide formation. The lower potential limit in the HER enhances the formation of the hydrous oxide by partially reducing the anhydrous oxide layer formed at higher potentials. The upper potential limit in the OER regime produces the required

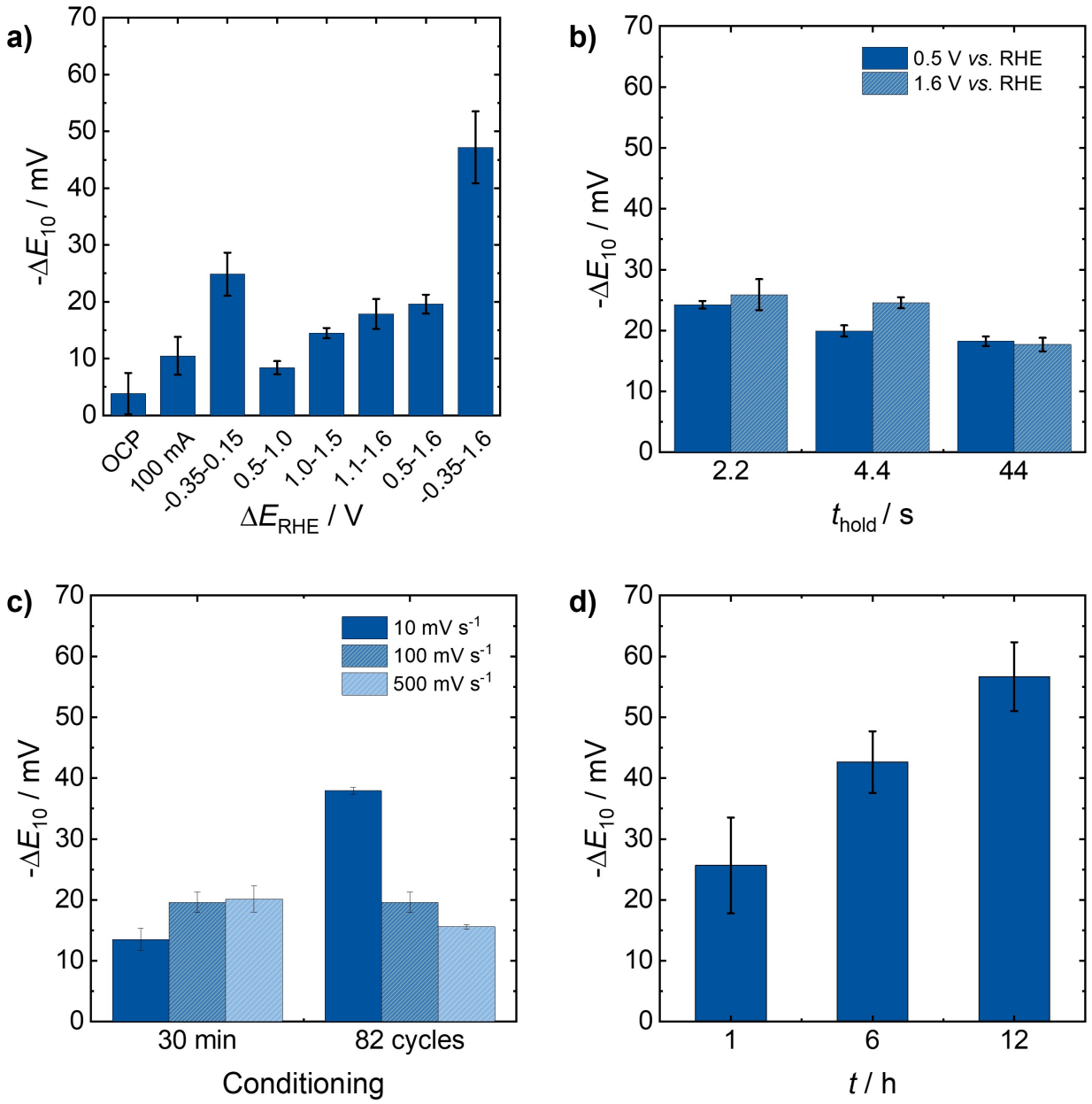

Figure 2. a-d) Activation ($-\Delta E_{10}$: potential difference at 10 mA cm^{-2} before and after conditioning) of $Ni_{70wt\%}Fe_{30wt\%}$ resulting from different conditioning. a) Conditioning for 30 min at OCP, 100 mA, and by CV with different potential limits. Conditioning time and scan rate are constant at 30 min and 100 mV s^{-1}. b) CV conditioning with different hold times at the upper (1.6 V) and lower (0.5 V) potential limit. Conditioning scan range, scan rate, and time are constant at 0.5–1.6 V, 100 mV s^{-1}, and 30 min. c) CV conditioning at different scan rates for a fixed conditioning time of 30 min and a fixed number of 82 CV cycles. Conditioning was performed in the potential range of 0.5–1.6 V. With the time fixed to 30 min, 9, 82, and 402 CV cycles were completed for 10, 100, and 500 mV s^{-1}, respectively. d) CV conditioning for 1, 6, and 12 h, which corresponds to 804, 4819, and 9638 cycles. Conditioning scan range and scan rate are constant at 0.5–1.6 V and 500 mV s^{-1}.

multilayer of (an)hydrous oxide and ensures deep penetration of oxygen.

For an increased focus on the upper and lower potential limits, the effect of introducing hold times at these potential limits was investigated. A schematic representation of the potential profiles is illustrated in Figure S5. Figure 2b shows the resulting activation. A slightly decreasing trend for the activation with increasing hold times can be seen, independent of the potential during the hold time. This is in line with the results in Figure 2a, where little to no significant activation at constant operation at higher (100 mA cm^{-2}) and lower (OCP) potentials could be observed. This supports the hypothesis that potential cycling is decisive for efficient surface oxidation. Thus, for a fixed conditioning time, the number of cycles showed a superior influence compared to the additional reduction/oxidation occurring at the lower or upper potential limits.

When the conditioning time is fixed, the number of cycles can alternatively be varied by the scan rate. Figure 2c shows the influence of the scan rate on the activation of the $Ni_{70}Fe_{30}$ electrode when cycling for a constant time of 30 min or a

constant number of 82 CV cycles. When conditioning for a constant time, the activation increases from 14 ± 2 mV at 10 mV s^{-1} to 20 ± 3 mV at $\geq$100 mV s^{-1}. When conditioning for a constant number of 82 CV cycles, this trend is reversed, and the conditioning at 10 mV s^{-1} with 38 ± 1 mV outperforms the activation when conditioning at 100 and 500 mV s^{-1}. This corresponds to an increased oxide growth per cycle for lower scan rates, which is in line with the reported results on the formation of an(hydrous) oxide films on Ni and Fe electrodes.[20,21,24] The saturation of the activation with increasing scan rate when conditioning for a fixed time illustrates the trade-off between increased oxide growth per cycle and the absolute oxide growth, which also depends on the total number of cycles.

To assess the impact of conditioning time or rather the number of cycles, the conditioning was extended to 12 h. Conditioning was performed between 0.5–1.6 V at 500 mV s^{-1}. The resulting activation in dependence on the time can be seen in Figure 2d. An increase of activation with time from 26 ± 8 mV after 1 h to 57 ± 6 mV after 12 h was observed. Although the activation from 6 h to 12 h was less than for the first 6 h, a final saturation after 12 h is not yet visible, suggesting that an ongoing activation with further cycling would be possible.

Summarizing, we found the conditioning for $Ni_{70}Fe_{30}$ would yield the largest activation when performing CV cycling between −0.35–1.6 V at 10 mV s^{-1} for a high number of cycles ($\geq$50). For a fixed conditioning time of 30 min, a high scan rate ($\geq$100 mV s^{-1}) without hold times at the upper or lower potential limit was beneficial.

Effect of Fe Content in Electrode and Electrolyte

Based on the optimization of the conditioning for $Ni_{70}Fe_{30}$ as a model electrode, the identified trends were applied to Ni- and Ni–Fe-electrodes with varying Fe-content. Figure 3 compares the activation of $Ni_{99.99}$ and $Ni_{70}Fe_{30}$ resulting from CV-conditioning with three different sequences, each for a) 46 cycles and b) 30 min. The conditioning was performed between two different potential windows, −0.35–1.6 V and 0.5–1.6 V, at 100 mV s^{-1} and at two different scan rates, 10 and 100 mV s^{-1}, for −0.35–1.6 V. In Figure 3a, for a constant number of cycles, the activation of $Ni_{99.99}$ and $Ni_{70}Fe_{30}$ shows the same trend. Namely, the highest activation is found for the largest potential window with low scan rate (−0.35–1.6 V, 10 mV s^{-1}), followed by the same potential window with higher scan rate (−0.35–1.6 V, 100 mV s^{-1}), and lastly the smaller potential window with the higher scan rate (0.5–1.6 V, 100 mV s^{-1}). This trend is in line with the conditioning optimization for $Ni_{70}Fe_{30}$. Interestingly, similar trends can be observed for various Ni–Fe compositions (compare Figure S6) and were also reported for the conditioning of different steels, as well as pure Ni and Fe.[20–24,34,43] Upon closer examination, it becomes apparent that the impact of the lower potential limit on the activation is more pronounced for $Ni_{70}Fe_{30}$ in contrast to $Ni_{99.99}$. Possibly, this potential regime favors Fe dissolution. As we found that for our Ni–Fe alloys 10–20 wt% Fe are favorable for the absolute activity (Figure S7), the

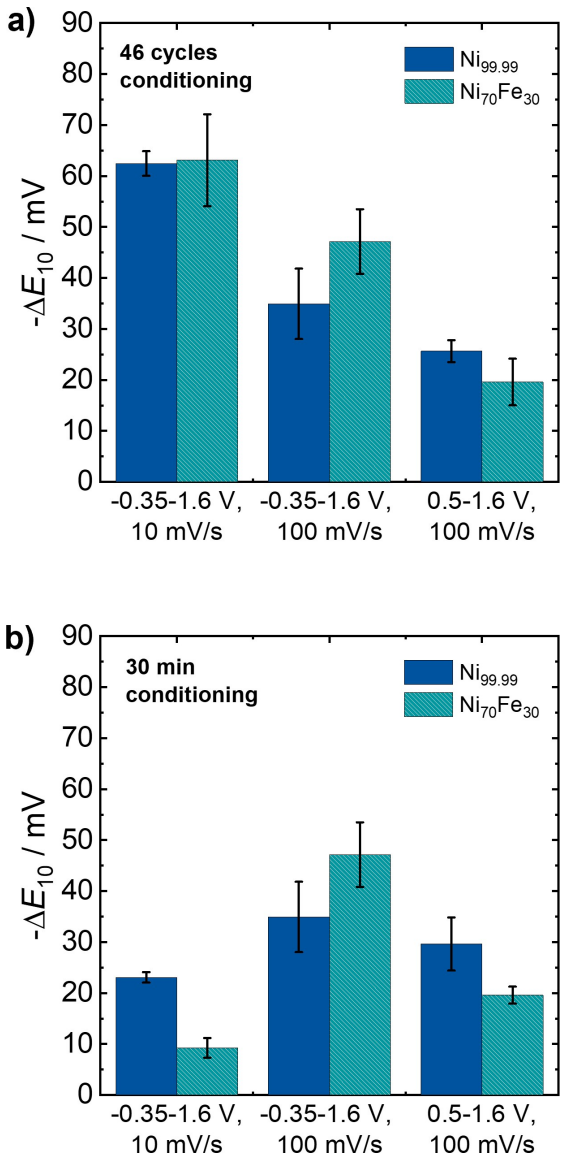

Figure 3. Activation ($-\Delta E_{10}$: potential difference at 10 mA cm^{-2} before and after conditioning) of $Ni_{99.99}$ and $Ni_{70}Fe_{30}$ resulting from CV-conditioning between −0.35-1.6 V at 10 mV s^{-1}, −0.35-1.6 V at 100 mV s^{-1}, and 0.5-1.6 V at 100 mV s^{-1} for a) 46 cycles and b) 30 min. With a fixed time of 30 min, 82 (0.5–1.6 V, 100 mV s^{-1}), 46 (−0.35–1.6 V, 100 mV s^{-1}), and 5 (−0.35–1.6 V, 10 mV s^{-1}) CV cycles were performed. Experiments were performed in 1 M KOH at room temperature.

Fe-dissolution from $Ni_{70}Fe_{30}$ during conditioning results not only in a larger active surface area but also in a slightly more beneficial Ni:Fe ratio. Comparing the different scan rates, we can see that the difference between the activation at 10 and 100 mV s^{-1} is larger for $Ni_{99.99}$ than for $Ni_{70}Fe_{30}$. This indicates that the activation of $Ni_{99.99}$ is kinetically more hindered, either by a slower oxidation process or mass transport through the oxide layer.

For a constant time of 30 min, as depicted in Figure 3b, a different trend is observed. Here, the highest activation resulted when conditioning with the large potential window at a high scan rate (−0.35–1.6 V, 100 mV s^{-1}), followed by the smaller potential window at the same scan rate (0.5–1.6 V, 100 mV s^{-1}),

and lastly the large potential window at the low scan rate (−0.35–1.6 V, 10 mV s^{-1}). The order is changed since the number of cycles varies between the different conditionings. 82 (0.5–1.6 V, 100 mV s^{-1}), 46 (−0.35–1.6 V, 100 mV s^{-1}), and 5 (−0.35-1.6 V, 10 mV s^{-1}) CV cycles were performed for the respective conditioning. This explains why the smallest activation resulted for the conditioning with 10 mV s^{-1} since here the number of cycles is an order of magnitude lower than for the other two. Interestingly, the activation of $Ni_{99.99}$ is approximately double that of $Ni_{70}Fe_{30}$ under these conditions. This hints at the activation of $Ni_{99.99}$ increasing more rapidly within the first few cycles. Comparing the two potential windows, it becomes evident that for $Ni_{70}Fe_{30}$, the lower potential limit demonstrates a more substantial impact on the activation than a higher frequency of cycles over the Ni redox peak. For $Ni_{99.99}$, the increased cycling over the Ni redox peak shows a similarly beneficial effect as conditioning with a lower potential limit and a reduced number of cycles. This supports the hypothesis that the importance of the lower limit for the activation depends on the amount of Fe content in the electrode.

The activation of $Ni_{99.99}$, $Ni_{99.2}$, $Ni_{90}Fe_{10}$, $Ni_{80}Fe_{20}$, and $Ni_{70}Fe_{30}$, resulting from CV-conditioning with the same sequences shown in Figure 3b, is compared in Figure S6 in the Supporting Information. For all materials, the same trends as in Figure 3b were found. Figure S6 identifies that $Ni_{99.99}$ and $Ni_{99.2}$ perform the same, as well as the Ni–Fe-alloys among one another. Similarly as in Figure 3b, the activation of Ni is more than double compared to all Ni–Fe-alloys at the low scan rate. Also in line with Figure 3b, the lower potential limit shows a larger impact on the activation of the Ni–Fe-alloys than a higher frequency of cycles over the Ni redox peak. Interestingly, activation increases with rising Fe-content in the electrode when conditioning between −0.35–1.6 V at 100 mV s^{-1}. This supports the hypothesis that the lower potential limit is of increasing importance for the activation with rising Fe content in the electrode. This could be attributed to an increased Fe dissolution in electrodes with higher Fe content. The Fe dissolution might result in a greater surface area and a subtle improvement in the Ni : Fe ratio.

To validate this hypothesis, the Fe dissolution was investigated *in-situ* by inductively coupled plasma optical emission spectroscopy (ICP-OES) during the conditioning of $Ni_{70}Fe_{30}$ between −0.35–1.6 V and 0.5–1.6 V. Therefore, three analysis CVs at a scan rate of 2 mV s^{-1} were performed, followed by a 30 min conditioning at 100 mV s^{-1}, and lastly again an analysis CV at 2 mV s^{-1}. K was measured as internal standard. The Fe and K concentrations for the entire sequence can be seen in Figure S9. The K spectrum shows a stable electrolyte concentration over the course of the experiment for both sequences. The sharp intensity drops are associated with gas evolution. The Fe spectrum shows a constant Fe concentration over most of the experiment. Only during the first analysis CV and during the 30 min CV conditioning between −0.35–1.6 V a significant Fe dissolution is visible. Thus, Figure 4 focusses on a) the first analysis CV and b) the 30 min conditioning at 100 mV s^{-1}. Figure 4a shows that Fe dissolution occurs during the oxidative potential sweep between 0.3–1.2 V. As the conditioning between 0.5–1.6 V covers only a part of this potential window, the Fe dissolution appears to be smaller compared to the conditioning between −0.35–1.6 V. This enhanced Fe dissolution for the conditioning between −0.35–1.6 V becomes more evident when comparing the course of the Fe concentration during the CV conditioning at 100 mV s^{-1} for 30 min in Figure 4b. While the Fe concentration stays constant at 116 ppb when conditioning between 0.5–1.6 V, the Fe concentration increases to approx. 121 ppb when cycling between −0.35–1.6 V. This supports the hypothesis that conditioning with −0.35 V as lower potential limit enhances Fe dissolution for Ni–Fe electrodes. This might then result in a greater surface area and a subtle improvement in the Ni : Fe ratio.

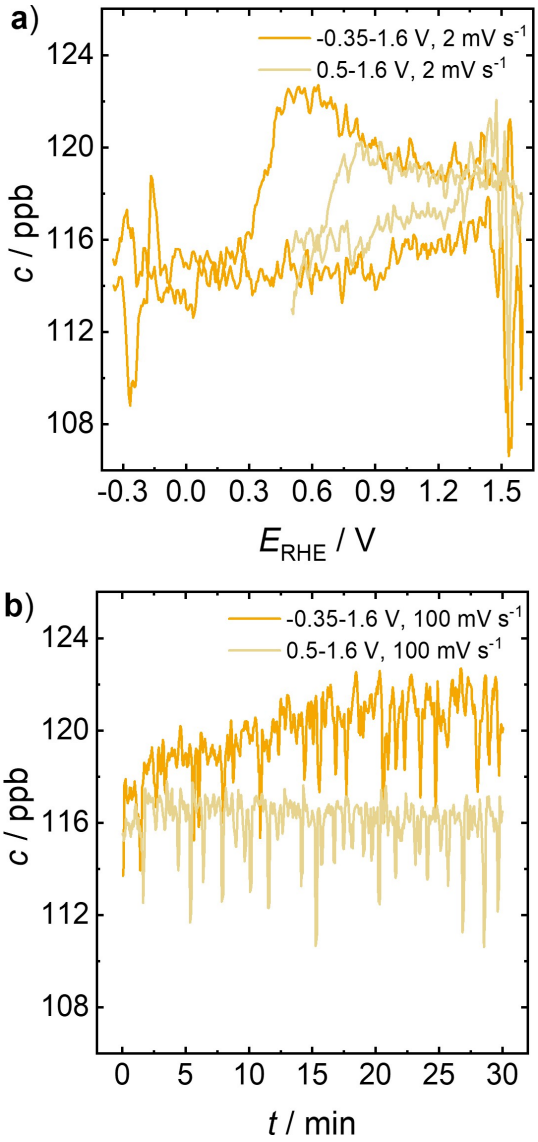

Figure 4. Fe concentration measured *in-situ* while performing a) CV at 2 mV s^{-1} and b) CV conditioning at 100 mV s^{-1} on $Ni_{70}Fe_{30}$. CV was conducted between −0.35–1.6 V and 0.5–1.6 V. Experiments were performed in 1 M KOH at room temperature.

In addition to varying the Fe-content in the electrode, we investigated the impact of different Fe-contents in the electro-

lyte on activity and activation. Figure 5 displays the OER potential at 10 mA cm^{-2} for $Ni_{99.99}$ and $Ni_{70}Fe_{30}$ before and after CV-conditioning at different Fe concentrations. Conditioning was performed between −0.35–1.6 V at 100 mV s^{-1} for 30 min (=46 cycles). The Fe concentrations were set to approx. 10, 120, and 1120 ppb. For the previous discussed conditioning optimization of $Ni_{70}Fe_{30}$, 1 M KOH with 120 ppb Fe was used. In Figure 5, it is evident that at very low Fe concentrations in the electrolyte of approx. 10 ppb, the potential of unconditioned $Ni_{99.99}$ is very high at 1.84 ± 0.01 V in contrast to Fe concentrations larger than 100 ppb. At Fe concentrations of 120 ppb and 1120 ppb, no significant differences in potentials were observed within the margin of error, resulting in an average potential of approx. 1.59 ± 0.03 V. It is important to note that determining the potential at 10 ppb Fe proved challenging as the potential increased significantly during its 10 min measurement time, as shown in Figure S8. This indicates an instability of the electrode-electrolyte interface. Such pronounced deactivation was not observed for the electrolytes with higher Fe concentrations. After conditioning, the potential increase at 10 ppb Fe was minimized. The final potential at 10 ppb Fe was, however, still 100 mV higher than for electrolytes containing ≥120 ppb, where an average potential of 1.56 ± 0.03 V was obtained (Figure 4 as well as Figure S8). This suggests that Fe incorporation and stabilization of a dynamic Fe equilibrium might be difficult during constant current operation for $Ni_{99.99}$ at 10 ppb without conditioning. During conditioning, a slight Fe incorporation might occur and stabilize the surface-electrolyte interface. This aligns with previous reports, which state that the activity of Ni only depends on the Fe concentration for concentrations smaller than 100 ppb[46] and that a stable dynamic Fe-dissolution-redeposition equilibrium is required for stable OER performance.[46,47]

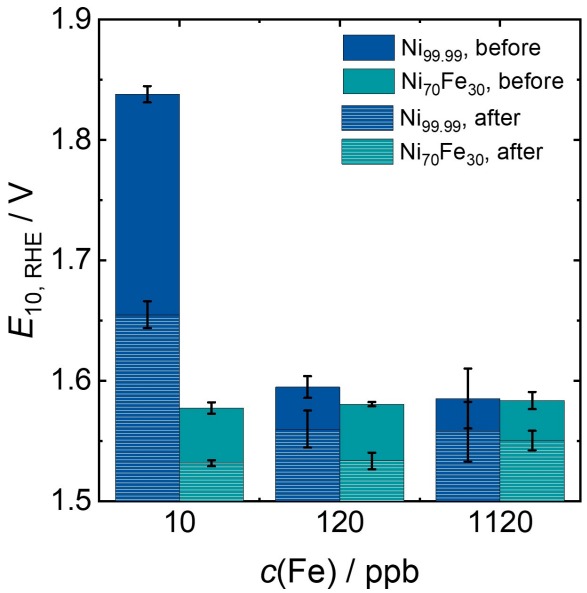

Figure 5. Potential at 10 mA cm^{-2}, $E_{10,RHE}$, before and after CV-conditioning with different Fe concentrations of approx. 10, 120, and 1120 ppb in the electrolyte. Conditioning was performed between −0.35–1.6 V at 100 mV s^{-1} for 30 min (=46 cycles). Experiments were performed in 1 M KOH at room temperature.

For $Ni_{70}Fe_{30}$, the potential before conditioning of 1.58 ± 0.01 V is unaffected by changes in Fe concentrations. This suggests that there is enough Fe present to ensure a stable dynamic Fe-equilibrium at the electrode surface. At low Fe concentrations, the local Fe concentration might be increased by Fe dissolution from the Ni–Fe-alloy. While the activation with Fe concentrations of 10 and 120 ppb are similar with 46 ± 7 mV for 10 ppb and 47 ± 6 mV for 120 ppb, the activation in an electrolyte with 1120 ppb Fe is lower with 33 ± 2 mV. A possible explanation might be that at these high Fe concentrations, less Fe dissolution occurs, resulting in a smaller increase of active surface area by conditioning.

Induced Surface Changes by Conditioning

To better understand the processes occurring during conditioning, $Ni_{99.99}$ and $Ni_{70}Fe_{30}$ electrodes were conditioned with the optimized 30 min-protocol (−0.35–1.6 V, 100 mV s^{-1}, 46 cycles) and were analyzed by optical microscopy, SEM, EDX, and XPS before and after conditioning.

Figure S10 shows that microscopically, no grown structures or changes are visible at a scale of 50 μm. Macroscopically, the structure and color of the electrodes did change due to conditioning, as seen in Figure S10b, d, h, j. $Ni_{70}Fe_{30}$ showed a golden-brown color after conditioning, which was persistent for multiple days. $Ni_{99.99}$ was colored dark grey after conditioning. This coloration, however, disappeared in air within hours. The origin of the color of the conditioned $Ni_{70}Fe_{30}$ is unclear and probably results from the mixed Ni–Fe-oxides. For $Ni_{99.99}$, we can postulate, based on previous reports, that the dark grey color originates from NiOOH, which quickly decomposes in air without polarization.[48]

The elements Ni, Fe, and O were quantified by EDX before and after conditioning. Present C on the electrodes was disregarded, as it probably originates from atmospheric contamination. The results are summarized in Figure 6. The corresponding EDX spectra can be seen in Figure S11. Before conditioning, 0.3 ± 0.2 norm. at% and 0.7 ± 0.3 norm. at% O were detected for $Ni_{99.99}$ and $Ni_{70}Fe_{30}$, respectively. These small amounts of O could be surface oxidation due to exposure to air. The atomic Ni:Fe ratio for $Ni_{70}Fe_{30}$ was 2.1 ± 0.1, which corresponds to the calculated Ni:Fe ratio of 2.2 from stoichiometry. After conditioning, the O-content increased to 6.0 ± 0.7 norm. at% for $Ni_{99.99}$ and 7.5 ± 0.6 norm. at% for $Ni_{70}Fe_{30}$. The Ni:Fe ratio stayed constant for $Ni_{70}Fe_{30}$, and no Fe incorporation could be detected for $Ni_{99.99}$. This indicates that by conditioning, $Ni_{99.99}$ and $Ni_{70}Fe_{30}$ are oxidized, and the Ni:Fe ratio is not significantly affected. However, it needs to be noted that EDX is a bulk-sensitive method. This means that a slight metal dissolution or Fe deposition at the surface could have been missed as the EDX signal mostly represents the Ni:Fe ratio from the bulk.

To determine the surface composition and speciation of the electrodes, XPS measurements were carried out before and

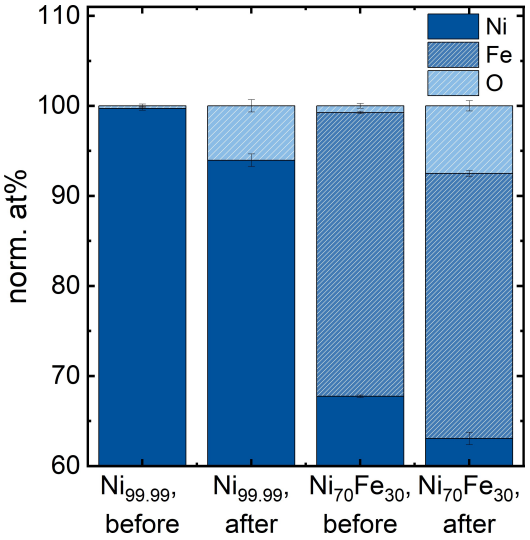

Figure 6. Average norm. at% of Ni, Fe, O detected by EDX for $Ni_{99.99}$ and $Ni_{70}Fe_{30}$ as polished and after conditioning. Conditioning was performed between −0.35–1.6 V at 100 mV s^{-1} for 30 min (=46 cycles). Experiments were performed in 1 M KOH at room temperature. The error bars represent the standard deviation resulting from three measurements on one electrode. The corresponding EDX spectra can be seen in Figure S11.

after conditioning. The resulting Ni 2p, Ni 3p, Fe 3p, and O 1s spectra are shown in Figure 7. The analysis of the Fe 2p core level peak was omitted due to its interference with the predominant $L_3M_{23}M_{45}$ Auger line of Ni under Al K_α X-ray radiation. The survey and C 1s spectra are depicted in Figure S12. In the Ni 2p spectra, shown in Figure 7a, the strong signal at a binding energy (BE) of 852.7 eV[49] corresponds to Ni^0 and proves the predominant metallic character of $Ni_{99.99}$ and $Ni_{70}Fe_{30}$ after polishing and before conditioning. The peaks at 856.3 eV[49] and 854.7 eV[49] indicate the presence of small amounts of $Ni(OH)_2$ and NiO, probably formed by exposure to air. When Fe acts as a ligand in NiO, the main Ni(Fe)O peak appears 1.6 eV above the pure NiO main peak.[50,51] Such a peak cannot be resolved in the present spectra as the peak is expected to be small and overlaying with the $Ni(OH)_2$ peak. Additionally, both NiO and $Ni(OH)_2$ peaks are shifted by 0.9 eV to higher binding energies compared to the literature. Since the corresponding peaks in the O 1s spectra and also the adventitious carbon in the C 1s spectra (see Figure S11) are similarly shifted, this shift can be attributed to the charging of the layers above the unconverted and uncharged Ni metal. After conditioning, $Ni_{99.99}$ and $Ni_{70}Fe_{30}$ show no contribution by the metallic species Ni^0 anymore, and only the peak at 856.3 eV with a small shoulder at 854.8 eV is visible. This indicates that by conditioning, the metal surface is completely oxidized within the measurement depth of the XPS (~10 nm).[52] The Ni 3p and Fe 3p spectra, seen in Figure 7b, were used to evaluate the Ni and Fe content at the surface. In the Ni 3p spectrum a strong signal at a BE of 66.2 eV with a shoulder at 67.5 eV was detected for both electrodes before conditioning. The lower peak is linked to Ni^0 and the higher peak to both its satellite peak and $NiO/Ni(OH)_2$.[49] After conditioning, only a peak at 68.4 eV with a shoulder at 73.4 eV was obtained for both electrodes, suggest-

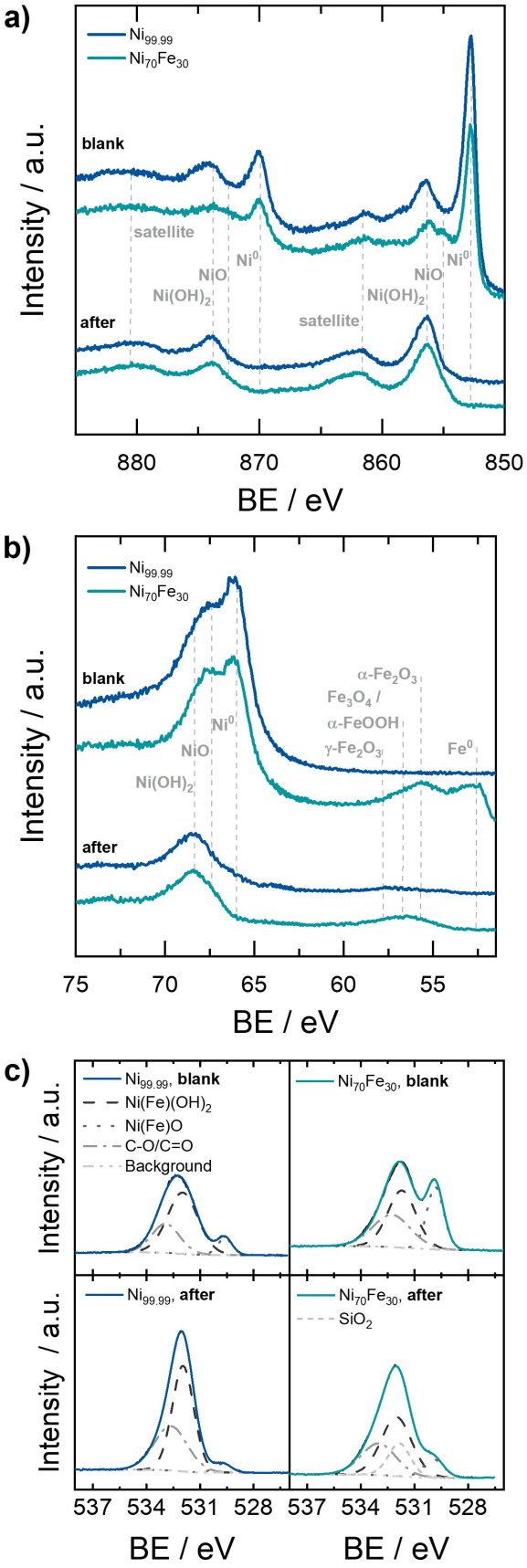

Figure 7. (a) Ni 2p, (b) Ni 3p, Fe 3p, c) O 1s XPS spectra for $Ni_{99.99}$ (blue) and $Ni_{70}Fe_{30}$ (petrol) measured *ex-situ* before and after conditioning. Conditioning was performed between −0.35–1.6 V at 100 mV s^{-1} for 30 min (=46 cycles). Experiments were performed in 1 M KOH at room temperature.

ing a complete surface oxidation within the XPS measurement depth, as also seen in the Ni 2p spectrum. The Fe 3p spectrum identifies metallic Fe and a mixture of various Fe-oxides, potentially α-Fe_2O_3, at a BE of 52.7 eV and 55.6 eV for $Ni_{70}Fe_{30}$ before conditioning.[49] For $Ni_{99.99}$, no Fe species were detected in the unconditioned state. After conditioning, metallic Fe^0 could no longer be detected for $Ni_{70}Fe_{30}$, and only a broad peak at 56.7 eV was obtained. This peak could correspond to multiple Fe-oxides, such as γ-Fe_2O_3 (57.8 eV), Fe_3O_4 (56.7 eV), or α-FeOOH (57.0 eV).[49] $Ni_{99.99}$ showed the same broad peak at 56.7 eV with little intensity, indicating Fe incorporation by conditioning. The Ni and Fe content was quantified by integrating the areas of the Ni 3p and Fe 3p spectra. For $Ni_{70}Fe_{30}$, the resulting Ni:Fe ratio increased from 2.4 to 3.0 by conditioning, suggesting a slight Fe dissolution. For $Ni_{99.99}$, Fe was incorporated with a Ni:Fe ratio of 10. The O 1s spectra in Figure 7c were used to quantify the oxide formation during conditioning and to resolve the metal hydroxide (M–OH) and metal oxide (M–O) present at the surface, which show peaks at 531.9 eV ($Ni(OH)_2$) and 529.8 eV (NiO, FeO), respectively.[49] The amount of surface oxides was quantified by relating the metal oxide and metal hydroxide peaks in the O 1s to the area of the Ni 3p and Fe 3p peaks. By conditioning, the O:M ratio increased by 29 at% for $Ni_{99.99}$ and 22 at% for $Ni_{70}Fe_{30}$. Also, the M–OH:M–O ratio rose from 7.5 to 15.6 for $Ni_{99.99}$ and from 1.5 to 4.9 for $Ni_{70}Fe_{30}$.

Overall, optical microscopy showed that no microscopic structure changes occurred at the electrode surfaces due to conditioning. Macroscopically, color and surface structure changes were observed and can potentially be attributed to the formed (oxyhydr)oxides. EDX and XPS spectra showed that by conditioning the metal surface was oxidized and the M–OH:M–O ratio was increased for both $Ni_{99.99}$ and $Ni_{70}Fe_{30}$. Additionally, Fe is incorporated when conditioning $Ni_{99.99}$, and Fe is dissolved for $Ni_{70}Fe_{30}$. We assume that the activating effect by surface oxidation is stronger than the adaptation of the Ni:Fe ratio, as the latter only accounts for small changes in the absolute activity (see Figure S7). This supports that the trends between the conditioning parameters and activation reflect the formation of a hydrous hydroxide layer.

Long-Term Stability of the Conditioning Effect

Lastly, we aimed to determine the sustainability of this activation process over time. Therefore, we tested an unconditioned and a conditioned $Ni_{70}Fe_{30}$ electrode at 100 mA cm^{-2} for 100 h and the results can be seen in Figure 8. Conditioning was performed between-0.35–1.6 V at 100 mV s^{-1} for 30 min (=46 cycles).

Figure 8 shows that for the unconditioned electrode, the potential started at 1.62 V, deactivated to 1.78 V after about 1.4 h and then dropped again to 1.76 V after approx. 7.1 h. Within the next 30 h, the potential increased rapidly. In the last 20, the potential increase decreased to 0.4 mV h^{-1} and the final potential after 100 h electrolysis was 1.94 V. The conditioned electrode, on the contrary, showed a stable performance with an initial potential of 1.58 V and a stable degradation rate of 0.4 mV h^{-1}. Consequently, with a final potential difference between the unconditioned and the conditioned electrode of 0.32 V after 100 h of electrolysis, it is evident that conditioning yields a beneficial impact on the electrode activity even in the long term. This indicates that while the formed hydrous oxide layer by CV conditioning is stable during constant current operation, the unconditioned electrode surface undergoes dynamic changes, which show first an activating and then a deactivating effect.

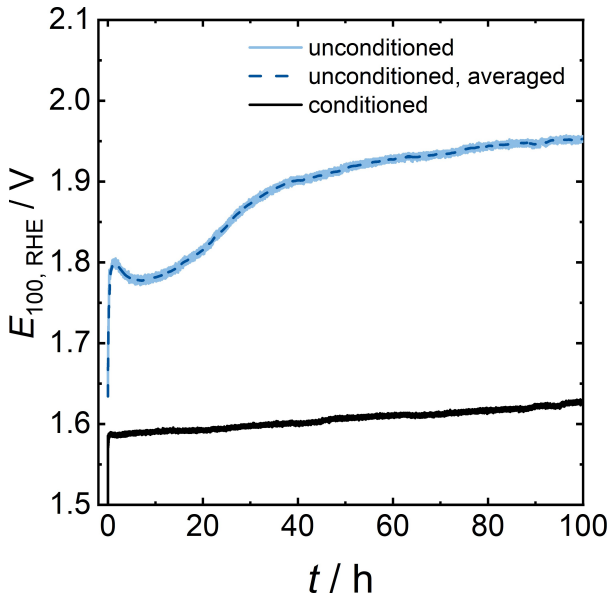

Figure 8. Long-term stability (100 mA cm^{-2} for 100 h) of an unconditioned and CV-conditioned $Ni_{70}Fe_{30}$ electrode. CV-conditioning was performed between −0.35–1.6 V at 100 mV s^{-1} for 30 min (46 cycles). Experiments were performed in 1 M KOH at room temperature.

Conclusions

In this work, we investigated systematically the correlation between activation, surface changes, and electrochemical conditioning parameters for Ni and Ni–Fe-electrodes with Ni:Fe ratios in the optimum regime. We found that for all materials, $Ni_{99.99}$, $Ni_{99.2}$, $Ni_{90}Fe_{10}$, $Ni_{80}Fe_{20}$ and $Ni_{70}Fe_{30}$, activation was greatest, if conditioning was performed with a high upper (1.6 V) and a low lower (−0.35 V) potential limit, a slow (10 mV s^{-1}) scan rate and many (≥50) cycles. For a fixed conditioning time, there is a trade-off between efficient oxide growth per cycle and the number of cycles being performed. Thus, depending on how much time is available, the optimum scan rate might vary. For 30 min, higher scan rates (≥100 mV s^{-1}) were beneficial. The conditioning led to outstanding improvements in electrochemical performance. For a 30 min-conditioning, the largest activation of 47±6 mV occurred when conditioning between −0.35–1.6 V at 100 mV s^{-1}. We could demonstrate the long-term stability of this conditioning effect, underlining its practical relevance. After 100 h, the conditioned electrode displayed a

potential 0.32 V lower than that of the unconditioned electrode, corresponding to a performance boost of more than 20%.

We suggest that the correlations between activation and conditioning parameters result primarily from surface oxidation and that Fe incorporation or dissolution only plays a minor role in the differences in electrode activation. To investigate the degree of surface oxidation, we analyzed the electrodes with SEM, EDX, and XPS as polished and after conditioning. Overall, the formation of a hydroxide layer during the activation was confirmed. We hypothesize that the larger the formed hydrous hydroxide layer, the larger the activation. To study the role of Fe in the activation, the Fe content in the electrolyte was varied. If sufficient Fe was present in the electrolyte (c(Fe) $\geq$ 100 ppb), a variation in Fe concentration did not affect the potential or activation, indicating a stable dynamic Fe equilibrium.

Overall, our research unveils once more the game-changing impact of conditioning on electrochemical activity and contributes to its understanding. Our observed correlations can be used to tailor the oxides of any pre-catalyst to (re)activate them. Enhancing the OER efficiency through conditioning is vital for improving the catalysts' effectiveness throughout extended AWE processes, underscoring the critical role of conditioning in catalyst preparation and electrochemical characterization.

Experimental Section

Electrochemical Procedure

The experiments were conducted in a self-designed electrochemical flow cell, described in the Supporting Information (see Figure S1), with a Gamry 1010E or 3000 potentiostat. The 1 cm^2 electrodes are in parallel with a 3 mm spacing, and as counter electrode glassy carbon (SIGRADUR G Glassy Carbon, HTW) was used. The working electrode materials were purchased at HMW Hauner and the compositions are in wt%, if not stated otherwise. Ni–Fe-alloys were made from $Ni_{99.9}$ and $Fe_{99.99}$. For electrode preparation, the working electrode was ground (7000 grit size, Matador, STARCKE), polished with an alumina-water-slurry (MicroPolish Suspensions, MicroCloth Polishing pads, Buehler) with decreasing grain size (1 μm, 0.3 μm, 0.05 μm), ultrasonicated in ultrapure water (Type 1, 0.05 μS cm^{-1}) for 5 min, and dried. Experiments were conducted at room temperature, ambient pressure, and in 1 M KOH, prepared from ultrapure water and KOH pellets (min. 85.0% KOH, CHEMSOLUTE). For the experiment, the flow cell, sealed with 0.8 Nm, was aligned vertically for efficient gas removal from the electrodes. From the argon-purged reservoir, the electrolyte ran through the flow cell in a single pass with a volume flow of 3 mL min^{-1}(Ismatec Reglo Digital Pump, 4 channels à 12 rolls). The electrochemical protocol consisted of an activity measurement before and after the conditioning. The activity was determined by first performing electrochemical impedance spectroscopy (EIS) at open circuit potential (100 kHz–10 Hz, 10 mV_{rms}), followed by CV (1.0–1.6 V, 3 cycles) at 10 and 100 mV s^{-1} and a chronopotentiometry (CP) at 10 mA cm^{-2} for 10 min. The conditioning was performed for 30 min, if not stated otherwise. A schematic overview of the electrochemical protocol can be seen in Figure S2 in the Supporting Information. The potentials are reported *vs.* RHE (see Supporting Information for conversion) and are 100% iR-corrected with the resistance from the respective EIS measurement.

Characterization

SEM & EDX: Microstructural analysis of the electrodes was conducted by Scanning Electron Microscopy (SEM) using a Hitachi Schottky SU5000 FESEM. 3,000× magnification and an accelerating voltage of 15 kV was used. Elemental compositions were determined by using a Bruker EDX, coupled to the SEM, with the accelerating voltage set to 15 kV.

Optical microscopy: Optical microscopic images of the electrodes were taken by Keyence VHX7000 microscope at a magnification of 20× (E20, X20).

XPS: X-ray photoelectron spectroscopy (XPS) measurements were performed with a hemispherical energy analyzer from SPECS (PHOIBOS 150) as part of the DAISY-FUN ultra-high vacuum cluster tool. The spectra were acquired using monochromatic Al K_α radiation (hv = 1486.74 eV) in fixed analyzer transmission mode. The binding energy calibration of the system has an accuracy of 0.1 eV and was done using sputter-cleaned Ag. The pass energy was 20 eV for the survey scan and 10 eV for the core level spectra and the step size was 0.3 eV and 0.05 eV, respectively. Data analysis was performed with CasaXPS, version 2.3.22.22.[53] For the samples, where Ni metal was present, the calibration was done with the valence band spectrum to the Fermi edge E_F = 0 eV. All spectra that were used for quantitative analysis were fitted with a Shirley background. Peaks in the O 1s were fitted with a GL(30) line shape. The fitting of the O 1s spectra includes carbon and silicon compounds, the area of which was derived from the C 1s and Si 2p, respectively. For all intensity calculations, the relative sensitivity factors published by Scofield were taken.[54]

ICP-OES: ICP-OES was performed with an Agilent 5800 VDV ICP-OES system to determine the Fe concentrations in the KOH electrolyte. Axial viewing and automatic background correction were employed. The Fe signal was detected at wavelengths of 238.204 nm and 259.940 nm. Quantitative wavelength calibration was performed by standard addition with commercial 1 M KOH as solvent.

Acknowledgements

We acknowledge financial support from the German Federal Ministry of Education and Research (BMBF project "PrometH2eus", FKZ 03HY105A, 03HY105H). Moreover, we thank Christian Marcks for his support with the design of the flow cell. Open Access funding enabled and organized by Projekt DEAL.

Conflict of Interests

The authors declare no conflict of interest.

Data Availability Statement

The raw data is made available in the Zendo reposity and can be accessed here: https://doi.org/10.5281/zenodo.13347934.

Keywords: Alkaline Water Electrolysis · Electrocatalyst Preparation · In-situ Electrode Conditioning · Electrode Activation · Online Dissolution

[1] S. Klaus, M. W. Louie, L. Trotochaud, A. T. Bell, *J. Phys. Chem. C* **2015**, *119*, 18303.
[2] S. Klaus, Y. Cai, M. W. Louie, L. Trotochaud, A. T. Bell, *J. Phys. Chem. C* **2015**, *119*, 7243.
[3] M. Steimecke, G. Seiffarth, M. Bron, *Anal. Chem.* **2017**, *89*, 10679.
[4] R. Wang, C. Wang, S. Yin, Y. Peng, J. Chen, Y. Deng, J. Li, *Catal. Today* **2021**, *364*, 140.
[5] F. Le Formal, L. Yerly, E. Potapova Mensi, X. Pereira Da Costa, F. Boudoire, N. Guijarro, M. Spodaryk, A. Züttel, K. Sivula, *ACS Catal.* **2020**, *10*, 12139.
[6] H. Schäfer, S. Sadaf, L. Walder, K. Kuepper, S. Dinklage, J. Wollschläger, L. Schneider, M. Steinhart, J. Hardege, D. Daum, *Energy Environ. Sci.* **2015**, *8*, 2685.
[7] J. Wang, Y. Gao, H. Kong, J. Kim, S. Choi, F. Ciucci, Y. Hao, S. Yang, Z. Shao, J. Lim, *Chem. Soc. Rev.* **2020**, *49*, 9154.
[8] M. S. Burke, L. J. Enman, A. S. Batchellor, S. Zou, S. W. Boettcher, *Chem. Mater.* **2015**, *27*, 7549.
[9] F. J. Pérez-Alonso, C. Adán, S. Rojas, M. A. Peña, J. Fierro, *Int. J. Hydrogen Energy* **2014**, *39*, 5204.
[10] A. S. Batchellor, S. W. Boettcher, *ACS Catal.* **2015**, *5*, 6680.
[11] Z. Yin, R. He, Y. Zhang, L. Feng, X. Wu, T. Wågberg, G. Hu, *J. Energy Chem.* **2022**, *69*, 585.
[12] Z. Lu, W. Xu, W. Zhu, Q. Yang, X. Lei, J. Liu, Y. Li, X. Sun, X. Duan, *Chem. Commun. (Camb.)* **2014**, *50*, 6479.
[13] Z. Cai, D. Zhou, M. Wang, S.-M. Bak, Y. Wu, Z. Wu, Y. Tian, X. Xiong, Y. Li, W. Liu, S. Siahrostami, Y. Kuang, X.-Q. Yang, H. Duan, Z. Feng, H. Wang, X. Sun, *Angew. Chem. Int. Ed. Engl.* **2018**, *57*, 9392.
[14] Z. Lu, L. Qian, W. Xu, Y. Tian, M. Jiang, Y. Li, X. Sun, X. Duan, *Nano Res.* **2016**, *9*, 3152.
[15] J. Mohammed-Ibrahim, *J. Power Sources* **2020**, *448*, 227375.
[16] Y. Cao, Y. Su, L. Xu, X. Yang, Z. Han, R. Cao, G. Li, *J. Energy Chem.* **2022**, *71*, 167.
[17] L. D. Burke, E. J. M. O'Sullivan, *J. Electroanal. Chem. Interfacial Electrochem.* **1981**, *117*, 155.
[18] Y. J. Son, S. Kim, V. Leung, K. Kawashima, J. Noh, K. Kim, R. A. Marquez, O. A. Carrasco-Jaim, L. A. Smith, H. Celio, D. J. Milliron, B. A. Korgel, C. B. Mullins, *ACS Catal.* **2022**, *12*, 10384.
[19] F. Moureaux, P. Stevens, G. Toussaint, M. Chatenet, *Appl. Catal. B* **2019**, *258*, 117963.
[20] M. E. G. Lyons, R. L. Doyle, I. Godwin, M. O'Brien, L. Russell, *J. Electrochem. Soc.* **2012**, *159*, H932–H944.
[21] R. L. Doyle, I. J. Godwin, M. P. Brandon, M. E. G. Lyons, *Phys. Chem. Chem. Phys.* **2013**, *15*, 13737.
[22] S. Rebouillat, M. E. Lyons, M. P. Brandon, R. L. Doyle, *Int. J. Electrochem. Sci.* **2011**, 5830.
[23] R. L. Doyle, M. E. G. Lyons, *J. Electrochem. Soc.* **2013**, *160*, H142–H154.
[24] L. D. Burke, M. E. Lyons, *J. Electroanal. Chem. Interfacial Electrochem.* **1986**, *198*, 347.
[25] H. Bode, K. Dehmelt, J. Witte, *Electrochim. Acta* **1966**, *11*, 1079.
[26] L. Trotochaud, S. L. Young, J. K. Ranney, S. W. Boettcher, *J. Am. Chem. Soc.* **2014**, *136*, 6744.
[27] P. Zhou, H. Bai, J. Feng, D. Liu, L. Qiao, C. Liu, S. Wang, H. Pan, *J. Mater. Chem. A* **2023**.
[28] H. R. Zamanizadeh, S. Sunde, B. G. Pollet, F. Seland, *Electrochim. Acta* **2022**, 140561.
[29] N. Todoroki, T. Wadayama, *Electrochem. Commun.* **2021**, *122*, 106902.
[30] N. Todoroki, T. Wadayama, *ACS Appl. Mater. Interfaces* **2019**, *11*, 44161.
[31] H. Schäfer, D. M. Chevrier, P. Zhang, J. Stangl, K. Müller-Buschbaum, J. D. Hardege, K. Kuepper, J. Wollschläger, U. Krupp, S. Dühnen, M. Steinhart, L. Walder, S. Sadaf, M. Schmidt, *Adv. Funct. Mater.* **2016**, *26*, 6402.
[32] N. Todoroki, T. Wadayama, *Int. J. Hydrogen Energy* **2022**, *47*, 32753.
[33] G.-R. Zhang, L.-L. Shen, P. Schmatz, K. Krois, B. J. Etzold, *J. Energy Chem.* **2020**, *49*, 153.
[34] S. Zhu, C. Chang, Y. Sun, G. Duan, Y. Chen, J. Pan, Y. Tang, P. Wan, *Int. J. Hydrogen Energy* **2020**, *45*, 1810.
[35] N. M. Kubo, F. Ketter, S. Palkovits, R. Palkovits, *ChemElectroChem* **2024**.
[36] Y. Zuo, V. Mastronardi, A. Gamberini, M. I. Zappia, T.-H.-H. Le, M. Prato, S. Dante, S. Bellani, L. Manna, *Adv. Mater.* **2024**, e2312071.
[37] F. Moureaux, P. Stevens, G. Toussaint, M. Chatenet, *J. Power Sources* **2013**, *229*, 123.
[38] L. Magnier, G. Cossard, V. Martin, C. Pascal, V. Roche, E. Sibert, I. Shchedrina, R. Bousquet, V. Parry, M. Chatenet, *Nat. Mater.* **2024**, 1.
[39] De Nora, "De Nora electrodic package for Alkaline Water Electrolysis", can be found under https://denora.com/applications/H2-production-by-water-electrolysis.html, **2016** (accessed on: 01.02.2023).
[40] M. Alsabet, M. Grden, G. Jerkiewicz, *Electrocatalysis (N Y)* **2011**, *2*, 317.
[41] M. Alsabet, M. Grdeń, G. Jerkiewicz, *Electrocatalysis (N Y)* **2015**, *6*, 60.
[42] M. E. Lyons, A. Cakara, P. O'Brien, I. Godwin, R. L. Doyle, *Int. J. Electrochem. Sci.* **2012**, *7*, 11768.
[43] M. E. G. Lyons, M. P. Brandon, *Phys. Chem. Chem. Phys.* **2009**, *11*, 2203.
[44] L. D. Burke, T. Twomey, *J. Electroanal. Chem. Interfacial Electrochem.* **1984**, *167*, 285.
[45] L. D. Burke, T. Twomey, *J. Electroanal. Chem. Interfacial Electrochem.* **1984**, *162*, 101.
[46] D. Y. Chung, P. P. Lopes, P. Farinazzo Bergamo Dias Martins, H. He, T. Kawaguchi, P. Zapol, H. You, D. Tripkovic, D. Strmcnik, Y. Zhu, S. Seifert, S. Lee, V. R. Stamenkovic, N. M. Markovic, *Nat. Energy* **2020**, *5*, 222.
[47] Q. Zhang, W. Xiao, H. C. Fu, X. L. Li, J. L. Lei, H. Q. Luo, N. B. Li, *ACS Catal.* **2023**, 14975.
[48] J. Gallenberger, H. Moreno Fernández, A. Alkemper, M. Li, C. Tian, B. Kaiser, J. P. Hofmann, *Catal. Sci. Technol.* **2023**, *13*, 4693.
[49] B. V. Crist, *Handbook of Monochromatic XPS Spectra. Volume 2: Commercially Pure Binary Oxides*, XPS International LLC, **2005**.
[50] M. A. van Veenendaal, G. A. Sawatzky, *Phys. Rev. Lett.* **1993**, *70*, 2459.
[51] C. Gort, P. W. Buchheister, M. Klingenhof, S. D. Paul, F. Dionigi, R. van de Krol, U. I. Kramm, W. Jaegermann, J. P. Hofmann, P. Strasser, B. Kaiser, *ChemCatChem* **2023**, *15*.
[52] F. A. Stevie, C. L. Donley, *J. Vac. Sci. Technol. A* **2020**, *38*.
[53] N. Fairley, V. Fernandez, M. Richard-Plouet, C. Guillot-Deudon, J. Walton, E. Smith, D. Flahaut, M. Greiner, M. Biesinger, S. Tougaard, D. Morgan, J. Baltrusaitis, *Appl. Surf. Sci. Adv.* **2021**, *5*, 100112.
[54] J. H. Scofield, *J. Electron Spectrosc. Relat. Phenom.* **1976**, *8*, 129.
[55] J. N. Hausmann, B. Traynor, R. J. Myers, M. Driess, P. W. Menezes, *ACS Energy Lett.* **2021**, *6*, 3567.

Manuscript received: April 17, 2024
Revised manuscript received: June 20, 2024
Version of record online: August 30, 2024